Journal of The Electrochemical Society, **164** (13) D875-D887 (2017)
0013-4651/2017/164(13)/D875/13/$37.00 © The Electrochemical Society

Modeling and Analysis of Electrodeposition in Porous Templates

Alta Fang[a,z] **and Mikko Haataja**[b,z]

[a]*Department of Mechanical and Aerospace Engineering, Princeton University, Princeton, New Jersey 08544, USA*
[b]*Department of Mechanical and Aerospace Engineering, Princeton Institute for the Science and Technology of Materials (PRISM), the Andlinger Center for Energy and the Environment (ACEE), and Program in Applied and Computational Mathematics (PACM), Princeton University, Princeton, New Jersey 08544, USA*

Controlling the morphology of materials grown via electrodeposition into porous templates remains a challenge, since the filling of the template often proceeds in a non-uniform manner, which is undesirable for applications such as nanowire fabrication. Here, we first develop a continuum phase-field approach for modeling electrodeposition into a porous template. We simulate growth within a single straight pore in order to study the fraction of the pore width filled by the deposit under various conditions, and then simulate growth within and overflowing a template composed of several straight pores. We reproduce experimentally observed cap morphologies and corresponding current transients, and find that when the template material is permeable to ionic diffusion, growth becomes more non-uniform. We also perform simulations of electrodeposition in pores with cross-sectional areas that vary over the height of the template, and show that the deposit homogeneity is strongly affected by variations in pore geometry. Finally, we carry out a statistical analysis of length distributions of electrodeposited nanowires extracted from experimental images. Such an analysis enables us to quantify, e.g., the pore-to-pore variations in nucleation times or growth rates required to yield the observed spread in nanowire lengths.
 [DOI: 10.1149/2.1331713jes]

Manuscript submitted August 15, 2017; revised manuscript received October 3, 2017. Published October 26, 2017.

Introduction

Using electrodeposition to deposit materials into the long and narrow pores of porous templates is an efficient technique for fabricating nanowires,[1] which have applications in a variety of devices such as sensors,[2] high-density magnetic data storage devices,[3] thermoelectrics,[4] and optoelectronic systems.[5] Common templates for nanowire deposition include anodized aluminum oxide (AAO) and ion-track-etched membranes,[6,7] which feature a dense array of pores that are up to 100 microns long and tens to hundreds of nanometers in diameter.[7,8] A challenge faced during electrodeposition into these templates is that often, a small fraction of nanowires reach the end of the template before the others and then grow radially outwards, blocking growth in neighboring pores and leading to a non-uniform nanowire array with many short nanowires that do not span the template.[9,10] Maximizing the fraction of nanowires that span the template is desirable for many applications, which require electrical contact between the top and bottom of each nanowire. Improving the uniformity of electrodeposition in a porous membrane is also relevant for battery applications, where electrodeposition conditions are typically different from those modeled in this work but which nonetheless face a similar challenge of preventing the protruding growth of electrodeposits, since metal "dendrite" growth across the porous battery separator during charging can short-circuit the cell, leading to battery failure.[11]

Differences in the lengths of electrodeposited nanowires have been attributed to differences in nucleation times,[4,12] non-uniform pore lengths,[12,13] cracks in the template,[14] pore branching,[8] and other pore irregularities,[12,15] but theoretical studies of template-assisted electrodeposition have been limited to simple model geometries and often use different models to describe different stages of the electrodeposition process.[8,12,13,16–19] A one-dimensional (1D) analytical solution for the growth trajectory of a nanowire in a single pore has been obtained in the limit of entirely diffusion-limited growth,[12] but it neglects the effects of electrode kinetics or the interfacial energy of the electrolyte-electrodeposit interface. Phase-field models for electrodeposition that do account for these phenomena have been developed,[20–23] and a phase-field model has been used to study metal dendrite growth through a porous battery separator.[24] However, phase-field simulations of template-assisted nanowire electrodeposition have not until now been performed.

In this paper, we develop a phase-field model for electrodeposition into a porous template. We perform phase-field simulations of growth first in a single straight pore, then in a template composed of several straight pores, and finally in branched pores. We find that permeability of the pore walls to ionic diffusion leads to more non-uniform growth. Using 1D simulations of a corresponding sharp-interface model for electrodeposition, we show that the growth rate can be significantly affected by how the cross-sectional area of the pore varies with height in the template. In addition, we develop a framework for statistically analyzing nanowire length distributions, which may be extracted from experimental scanning electron microscope (SEM) images. We analyze whether length distributions are bimodal or unimodal, and we determine the pore-to-pore variations in nucleation times or growth rates that yield particular nanowire length distributions. We emphasize that our modeling approaches are not unique to electrodeposition in porous templates, but can be applied more broadly in systems with diffusion- or reaction-kinetics-limited growth in confined geometries.

Theoretical Approach

Our starting point is a model for potentiostatic electrodeposition under mixed diffusion and charge transfer control. We assume that there is an excess of supporting electrolyte so that we can neglect ionic migration,[25] and we also neglect convection within the porous template.[26] Specifically, the transport equations and associated boundary conditions along the moving deposit-electrolyte interface used in this work are as follows. In the electrolyte, the concentration of the depositing species, c, is obtained from

$$\frac{\partial c}{\partial t} = \vec{\nabla} \cdot (D\vec{\nabla} c), \qquad [1]$$

where D denotes the diffusivity, while at the electrodeposit-electrolyte interface,

$$i = i_0 \left(\exp\left[\alpha_1 \left(\frac{n\mathcal{F}\phi_{el}}{RT} + \frac{\gamma\kappa V_m}{RT} \right) \right] - \frac{c}{c_{eq}} \exp\left[-\alpha_2 \left(\frac{n\mathcal{F}\phi_{el}}{RT} + \frac{\gamma\kappa V_m}{RT} \right) \right] \right); \qquad [2]$$

$$i = -n\mathcal{F} D \vec{\nabla} c \cdot \hat{n}; \qquad [3]$$

$$v_n = \frac{-i}{c_s n\mathcal{F}}. \qquad [4]$$

That is, charge transfer kinetics at the electrode interface in Eq. 2 are modeled by the Butler-Volmer equation,[26–28] where i_0 denotes the

[z]E-mail: alta@princeton.edu; mhaataja@princeton.edu

exchange current density, α_1 and α_2 denote the charge transfer coefficients, c_{eq} denotes the equilibrium concentration of the depositing ion, V_m denotes the molar volume of the deposited material, κ denotes the interface curvature, γ denotes the electrolyte-electrodeposit interfacial energy, and n denotes the charge number of the depositing ion. The normal interfacial velocity v_n in turn is determined by the current density i and the effective molar volume of the deposit c_s^{-1} via Eqs. 3 and 4. Here we have assumed that electroneutrality holds throughout the electrolyte. We also confine our model to currents below the limiting current and ignore surface conduction effects or electroosmotic flow, which may become significant when the current exceeds the limiting current.[29]

Now, along the template walls whose material is impermeable to ionic diffusion,

$$\vec{\nabla} c \cdot \hat{n} = 0 \qquad [5]$$

where $\hat{n}$ is the unit vector normal to the respective interface. In template materials with finite exchange of ions between adjacent pores (due to, e.g., the presence of small cracks in the template), on the other hand, we have

$$\frac{\partial c}{\partial t} = \vec{\nabla} \cdot (D_{wall} \vec{\nabla} c), \qquad [6]$$

where D_{wall} denotes an effective diffusivity describing transport through the wall.

We assume that the electric potential is ϕ_{el} throughout the conductive deposit and 0 in the electrolyte, since the electrolyte is well-supported (and hence we may neglect the Ohmic drop). Thus, a negative value of the applied potential ϕ_{el} leads to electrodeposition, while a positive value of ϕ_{el} leads to dissolution. Furthermore, in order to model phenomena such as stirring of the electrolyte or the presence of side reactions that locally reduce the reaction rate, we allow both i_0 and D to vary in space such that $i_0(\vec{r}) = \tilde{i}_0 f_i(\vec{r})$ and $D(\vec{r}) = \tilde{D} f_D(\vec{r})$, where $f_i(\vec{r})$ and $f_D(\vec{r})$ are prescribed based on the specific conditions and geometry of the system. In addition, we model a deposit with isotropic properties, although in principle anisotropic interfacial energy and kinetics can also be included.

Next, in order to efficiently solve the above moving boundary problem, we formulate a corresponding phase-field model that is based on existing phase-field models for electrodeposition.[22,30] To this end, we define an order parameter field $\xi(\vec{r}, t)$ such that $\xi = 1$ in the solid deposit phase and $\xi = 0$ in the electrolyte or template material. We also define a static order parameter $\psi(\vec{r})$ that describes the template geometry, where $\psi = 1$ in the electrolyte or deposit and $\psi = 0$ in the template material. We define non-dimensional variables $\bar{c} = \frac{c}{c_{eq}}$, $\bar{i} = \frac{i}{\tilde{i}_0}$, $\bar{t} = \frac{t\tilde{i}_0}{n\mathcal{F}Lc_{eq}}$, $\bar{x} = \frac{x}{L}$, $\bar{D} = \frac{Dn\mathcal{F}c_{eq}}{\tilde{i}_0 L}$, $\bar{\phi}_{el} = \frac{n\mathcal{F}\phi_{el}}{RT}$, $\bar{c}_s = \frac{c_s}{c_{eq}}$, and $\bar{\gamma} = \frac{\gamma V_m}{RTL}$, where L is the height of the porous template. Finally, the surface energy γ can be expressed in terms of phase-field parameters ϵ and W that control the width of the diffuse interface as $\gamma = \sqrt{\frac{\epsilon^2 W}{18}}$. Thus the non-dimensionalized phase-field equations are (bars have been omitted below for clarity):

$$\frac{\partial \xi}{\partial t} = \psi f_i(\vec{r}) \frac{1}{c_s} \sqrt{\frac{W}{18\epsilon^2}} ([\alpha_1 \exp(\alpha_1 \phi_{el}) + \alpha_2 c \exp(-\alpha_2 \phi_{el})] \times [\epsilon^2 \nabla^2 \xi - W g'(\xi)] - p'(\xi)[\exp(\alpha_1 \phi_{el}) - c \exp(-\alpha_2 \phi_{el})]); \qquad [7]$$

$$\frac{\partial c}{\partial t} = \vec{\nabla} \cdot \left(D(\vec{r}) \left[\psi + (1 - \psi) \frac{D_{wall}}{D} \right] (1 - \xi) \vec{\nabla} c \right) - p'(\xi) c_s \frac{\partial \xi}{\partial t}, \qquad [8]$$

where $g(\xi) = \xi^2(1 - \xi)^2$ and $p(\xi) = \xi^3(6\xi^2 - 15\xi + 10)$. Following Ref. 22, we have Taylor expanded the exponentials in the Butler-Volmer equation in Eq. 2 assuming $\frac{\gamma \kappa V_m}{RT} \ll 1$ in order to maintain computational stability.

The phase-field equations above are solved numerically using finite differences on a regular grid in either two or three spatial dimensions. Explicit time-stepping is used for Eq. 7, while implicit Euler time stepping is used for Eq. 8. We employ periodic boundary conditions in the lateral direction, $\bar{c} = 1$ at the upper boundary, and zero-derivative boundary conditions at the lower boundary. We use representative non-dimensional parameters corresponding approximately to copper electrodeposition from a 0.5 M electrolyte solution into a 60-μm-thick AAO template: $\bar{c}_s = 280$, $\bar{D} = 10$, $n = 2$, $\bar{W} = 5$, $\bar{\epsilon}^2 = 1.75 \times 10^{-5}$, $\frac{D_{wall}}{D} = 0$ unless stated otherwise, and we assume $\alpha_1 = \alpha_2 = 0.5$. At the initial time, the deposit in each pore is nucleated with a hemispherical seed at the lower boundary and $\bar{c} = 1$ throughout the electrolyte.

Simulation Results

Three-dimensional phase-field simulations.—Figure 1a shows representative configurations from a three-dimensional (3D) phase-field simulation of electrodeposition into a template with a regular array of cylindrical pores. Here we set the growth rate to be greater in the central pore than in the other pores and model stirring of the electrolyte bath as described in more detail below. We use $\bar{\phi}_{el} = -10$ to model moderately diffusion-limited conditions. When the fastest-growing central nanowire reaches the end of the template, it forms a cap, similar to those observed experimentally.[12,31] We can also simulate electrodeposition in just one pore, as shown in Fig. 1b, and we observe that the growth of the nanowire accelerates over time, as expected when growth is subject to diffusion limitations. Next, in order to perform quantitative studies on larger computational domains, we focus on 2D simulations of growth within a single pore as well as in a template with many pores. We have found that 2D simulations exhibit the same qualitative behavior as 3D simulations and thus believe that results from our 2D simulations are also applicable to 3D geometries.

Fraction of pore width filled.—Motivated by experimental observations that electrodeposited nanowires can have diameters less than those of the pores in which they are deposited,[32,33] we use our phase-field model to perform simulations of electrodeposition in a single straight pore under various deposition conditions and observe the fraction of the pore width that is filled. Our simulation setup is illustrated in the schematic in Fig. 2a. We simulate pores of aspect ratio $\frac{L}{w} = 20$, where w is the width of the pore, which provides computational expedience while satisfactorily approximating the limit of $\frac{L}{w} \gg 1$. Although the system is never exactly in steady state, we observe that the width of the deposit w_d does not vary significantly over the length of a fully grown nanowire, so we report a single value for the fraction of pore width filled.

Here, we report the fraction of pore width filled as a function of non-dimensional parameters $\bar{\gamma}_w \equiv \frac{\gamma V_m}{wRT}$ and $\bar{D}_w \equiv \frac{Dn\mathcal{F}c_{eq}}{\tilde{i}_0 w}$. The parameter $\bar{\gamma}_w$ corresponds to the ratio of the capillary length to the pore width and typically has a value on the order of 10^{-2}.[34] First, we fix $\bar{\gamma}_w = 0.0118$ while varying $\bar{D}_w$ and $\bar{\phi}_{el}$. As shown in Fig. 2b, we find that the non-dimensional parameter $\bar{D}_w$, which is a measure of how diffusion-limited or reaction-kinetics-limited the growth is,[21,35] has a strong influence on the fraction of pore width filled. For systems that are more diffusion-limited, less of the pore width is filled, as expected since flatter growth fronts tend to become unstable under more diffusion-limited conditions. A transition from incomplete to complete pore filling occurs at approximately $\bar{D}_w = 2$. This is consistent with the fact that most experimentally reported electrodeposited nanowires completely fill the width of template pores, since in practice, usually $\bar{D}_w \gg 1$.

Furthermore, as shown in Fig. 2c, we find that as the non-dimensionalized electrode potential $\bar{\phi}_{el}$ becomes more negative, growth becomes more diffusion-limited and less of the pore width is filled, in agreement with experimental observations of $Bi_{1-x}Sb_x$ nanowire growth.[33] Finally, for fixed $\bar{D}_w = 0.5$, Fig. 2d shows that varying the interfacial energy of the electrodeposit-electrolyte interface also influences the fraction of pore width filled by the

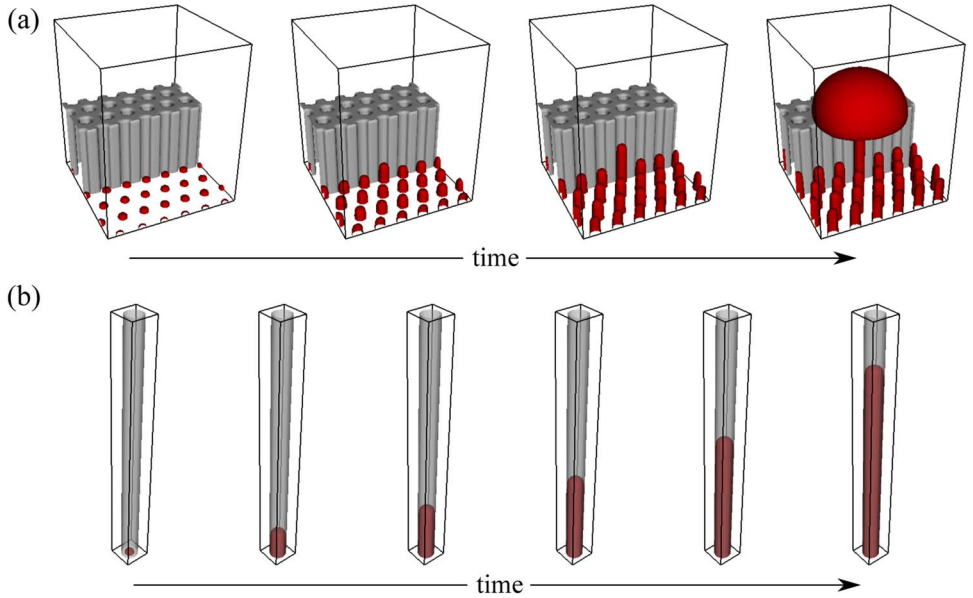

Figure 1. (a) Representative configurations from a 3D phase-field simulation of metal (red) electrodeposited into a porous template. The front half of the template (gray) is cut away for clarity. (b) Representative configurations from a 3D phase-field simulation of nanowire growth in a single cylindrical pore, whose wall is shown in translucent gray.

nanowire. For larger magnitudes of $\bar{\phi}_{el}$, which lead to more diffusion-limited growth, the trend resembles that of viscous fingering in Hele-Shaw cells, where the governing equations are similar to those here in the limit of entirely diffusion-limited growth.[36]

In summary, our simulations predict the conditions under which incomplete filling of the pore width occurs. We note that at large applied overpotentials, hollow nanotubes have been experimentally observed,[29,37] but our model cannot produce hollow structures since we do not account for hypothesized mechanisms such as surface conduction effects[29] or hydrogen bubble formation.[37]

Electrodeposition within and overflowing a template.—Next, we perform phase-field simulations of electrodeposition into and overflowing a template with many straight pores. In order to model the effect of stirring the electrolyte bath, we set the diffusivity of the electrolyte to be 20 times larger above the template than inside the pores.

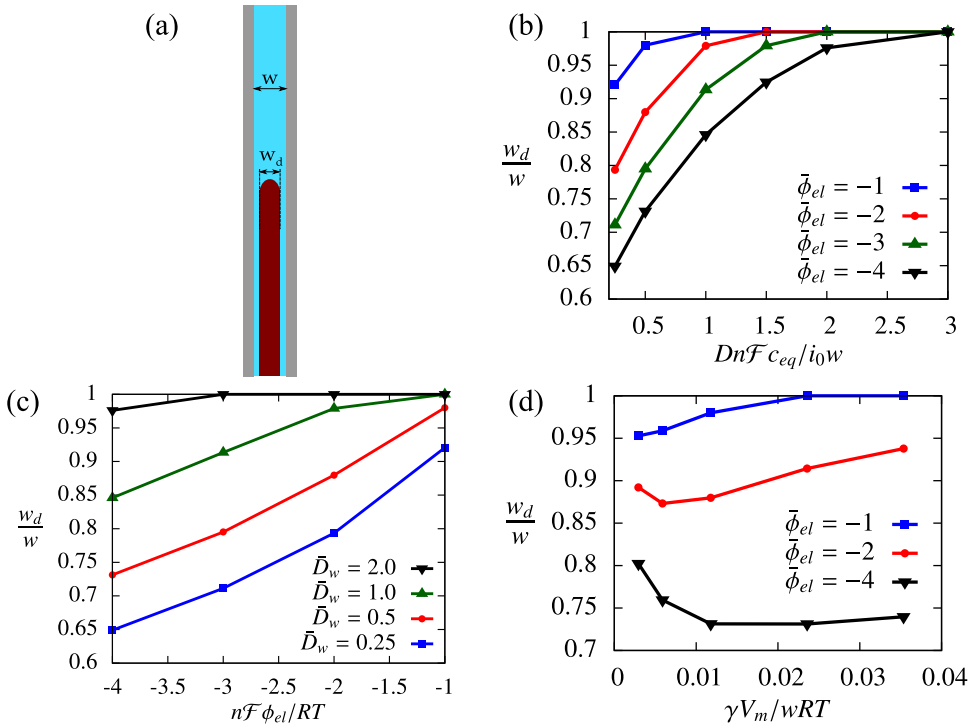

Figure 2. (a) Schematic of a nanowire (red) that does not completely fill the width of the pore, whose walls are shown in gray. (b) Fraction of pore width filled is plotted as a function of $\bar{D}_w$, (c) $\bar{\phi}_{el}$, and (d) $\bar{\gamma}_w$.

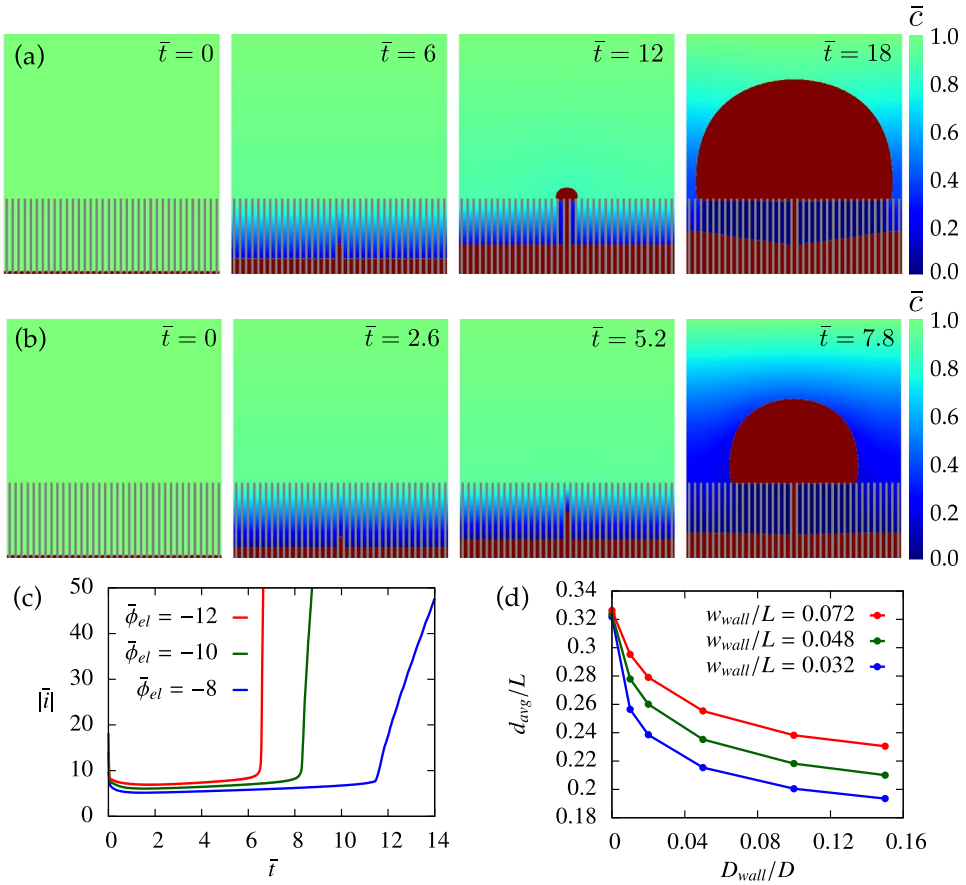

Figure 3. Representative configurations of phase-field simulations of electrodeposition into a template at various times, for (a) $\bar{\phi}_{el} = -8$ and (b) $\bar{\phi}_{el} = -12$. (c) Time evolution of the magnitude of the average current density, for various values of applied potential. (d) The average nanowire length decreases as the relative diffusivity of the template material increases and the pore wall thickness decreases.

We designate one pore at the center of the simulation to have a greater growth rate than the others by setting i_0 to be two times greater in the central pore than in all of the other pores, thereby modeling side reactions that reduce the reaction rate in all pores other than the central one by for example producing gas bubbles[38] or forming passivating surface layers. We have found that our simulations produce similar results when faster growth in the central pore is induced by either pore branching or a locally higher value of D instead of a locally higher value of i_0.

Figures 3a and 3b show series of representative configurations from phase-field simulations of electrodeposition into a template where $\bar{\phi}_{el} = -8$ and $\bar{\phi}_{el} = -12$ respectively. From these simulations we can determine the average current density as a function of time by tracking the total amount of material deposited as a function of time, assuming that all current is associated with deposit growth, and normalizing by the area of the template. As shown in Fig. 3c, the time evolution of the current density exhibits qualitative behavior similar to what has been observed experimentally.[8,15,18,19,39,40] The magnitude of the current density initially decreases as the diffusion layer expands, then increases slowly while the nanowires grow within the pores, and finally increases rapidly when the deposit overflows the template. In agreement with experiments,[8] a more negative applied potential results in shorter nanowires in the majority of pores due to the more diffusion-limited conditions that lead to greater acceleration during the growth process.

Next, we explore how a non-zero effective ionic diffusivity within the template material affects growth, since small cracks in the template may introduce the possibility of ionic diffusion between adjacent pores. Fixing $\bar{\phi}_{el} = -12$ in order to simulate highly diffusion-limited conditions, we vary the relative diffusivity of the pore walls $\frac{D_{wall}}{D}$ as well as the scaled pore wall thickness $\frac{w_{wall}}{L}$ and measure the resulting average scaled length $\frac{d_{avg}}{L}$ of the $n = 22$ nanowires surrounding the central fast-growing one. As shown in Fig. 3d, $\frac{d_{avg}}{L}$ decreases rapidly as $\frac{D_{wall}}{D}$ increases from 0, but this effect can be reduced by increasing the thickness of the pore walls. This reduction in nanowire length arises because growth of neighboring nanowires becomes competitive when ions are permitted to diffuse laterally between pores, as ionic current concentrates on the tips of longer nanowires at the expense of neighboring shorter nanowires. This shielding effect leads to a reduction in average nanowire length by amplifying discrepancies between the lengths of nanowires in adjacent pores. Furthermore, increasing the ionic diffusivity of the template material reduces overall ion transport limitations, leading to faster growth of the leading nanowire and earlier formation of the cap, which blocks further growth at an earlier time.

We also explore the effect of pore wall diffusivity on electrodeposition in templates with uniform growth conditions but with initial seed radii drawn from a normal distribution. Figures 4a and 4b show representative configurations over time from simulations where $\frac{D_{wall}}{D} = 0$ and $\frac{D_{wall}}{D} = 0.03$ respectively. Increasing the pore wall diffusivity broadens the distribution of nanowire lengths but does not introduce a separate second growth front, as demonstrated both in Fig. 4c, which shows the growth trajectories of each of the 40 nanowires in Fig. 4b, and in Fig. 4d, which shows the evolution of the nanowire length distribution over time for $\frac{D_{wall}}{D} = 0.03$ averaged over 15 simulations with different initial conditions. Pores that have overflowed to form caps are counted as $\frac{d}{L} = 1$. A characteristic effect of non-zero pore wall diffusivity is an anti-correlation of the lengths of nearest neighbor nanowires

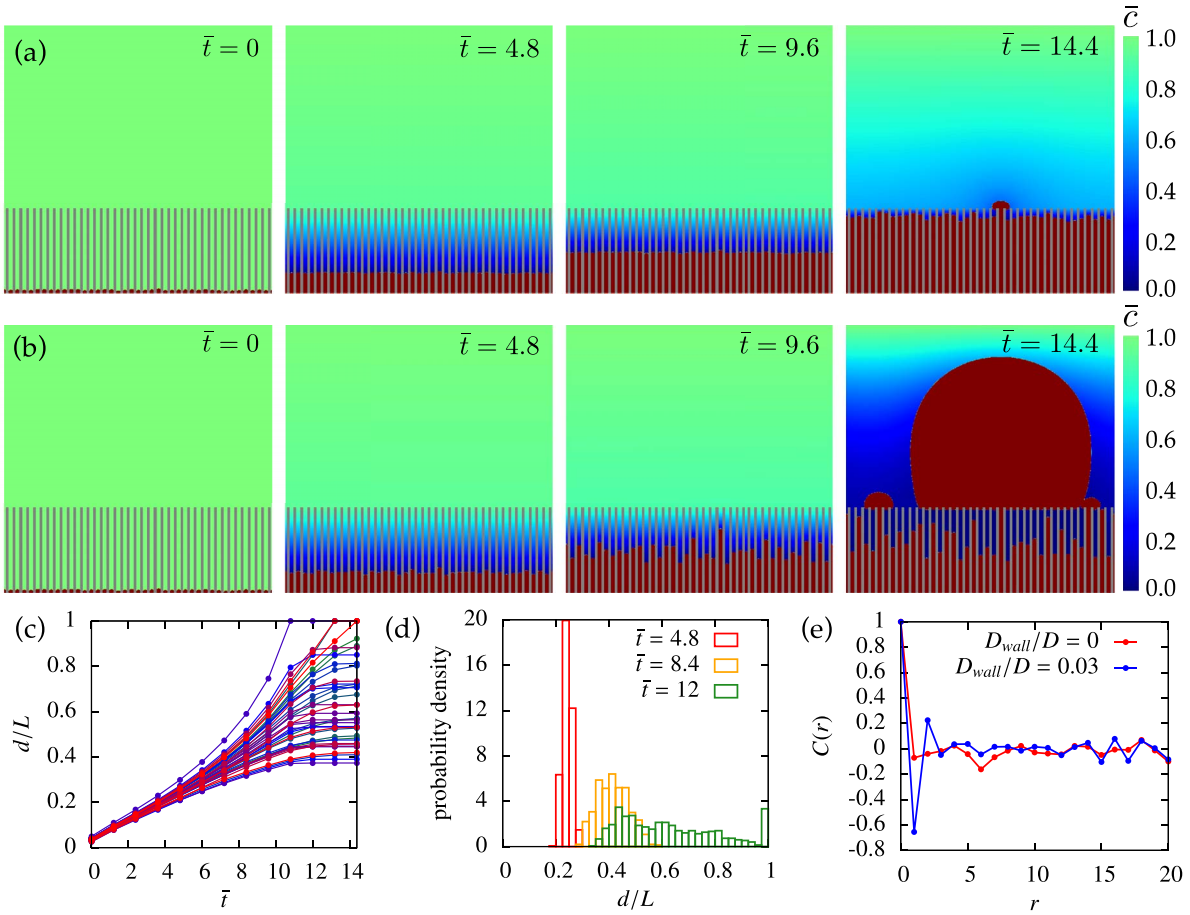

Figure 4. Representative configurations of phase-field simulations of electrodeposition into a template at various times, for (a) $\frac{D_{wall}}{D} = 0$ and (b) $\frac{D_{wall}}{D} = 0.03$. (c) Normalized nanowire length over time for each of the 40 nanowires in (b). Colors only distinguish trajectories and do not have any meaning. (d) Evolution of the nanowire length distribution over time for $\frac{D_{wall}}{D} = 0.03$, averaged over 15 simulations with different initial conditions. (e) Averaged autocorrelation coefficient as a function of number of pores apart r, showing anti-correlation of nearest neighbors when $\frac{D_{wall}}{D} > 0$.

due to competitive growth. Figure 4e plots the autocorrelation coefficient $C(r) = \frac{\sum_{i=1}^{N}(d_i - d_{avg})(d_{i+r} - d_{avg})}{\sum_{i=1}^{N}(d_i - d_{avg})^2}$ of the nanowire lengths at $\bar{t} = 14.4$ averaged over 15 simulations with different initial conditions, where r is the number of pores apart and periodic boundary conditions are accounted for. When the pore walls are impermeable to ionic diffusion, $C(r \geq 1)$ takes on small values, indicating lengths are uncorrelated, whereas when the pore wall diffusivity is greater than zero, $C(r = 1)$ is significantly negative, indicating anti-correlation of neighboring nanowire lengths. Our results suggest that if there is indeed non-zero ionic diffusion within the template material, then strategies to reduce pore wall diffusion such as applying compressive stress to the template or increasing the thickness of pore walls may lead to an increase in average nanowire length and homogeneity.

Effect of variations in pore cross-sectional area over the template height.—Next, we study the effect of template morphology on the growth of the electrodeposit. Pore branching is a commonly observed defect in commercial AAO membranes that has been hypothesized to cause differences in nanowire lengths.[8] Pore diameters are also often non-uniform over the height of the membrane,[15] and pores of varying cross-sectional area have been intentionally fabricated experimentally in ion-track-etched membranes.[6] Representative configurations from 2D phase-field simulations are shown in Fig. 5. Growth is faster when the total cross-sectional area increases with distance from the bottom of the template, whereas growth is slower if the total cross-sectional area decreases with height. As we shall see below, this effect can be attributed to the vertical asymmetry of the pore cross-sectional area, since a greater cross-sectional area in the upper part of the pore leads to a lower diffusional resistance for a greater duration of the growth process and therefore faster overall growth compared to a pore with oppositely distributed cross-sectional area.

To study in greater detail the effects of pore cross-sectional area variations, we perform 1D numerical simulations of the Fick-Jacobs equation,[41,42] which describes effective 1D diffusion in a 3D pore with cross-sectional area profile $A(z)$ and impermeable walls:

$$\frac{\partial \hat{c}}{\partial t} = \frac{1}{A(z)} \frac{\partial}{\partial z} \left(DA(z) \frac{\partial \hat{c}}{\partial z} \right). \quad [9]$$

Here, $\hat{c}$ denotes the concentration at z averaged over the cross-sectional area. The Fick-Jacobs equation is an accurate description of diffusion in a 3D channel when the pore is long enough that the concentration equilibrates much faster in the transverse direction than along the length of the pore, and the pore width does not vary too rapidly as a function of z.[41,42]

Assuming entirely diffusion-limited conditions and $\frac{c_s}{c_{eq}} \gg 1$ so that the concentration approximately attains its steady-state profile at each time, we derive that the time t_c to fill a pore with cross-sectional area profile $A(z)$, relative to the pore-filling time of a straight pore $t_{c,straight}$, is given by (see Appendix A for the derivation)

$$\frac{t_c}{t_{c,straight}} \equiv s = \frac{2}{L^2} \int_0^L \left(A(z) \int_z^L \frac{1}{A(z')} dz' \right) dz. \quad [10]$$

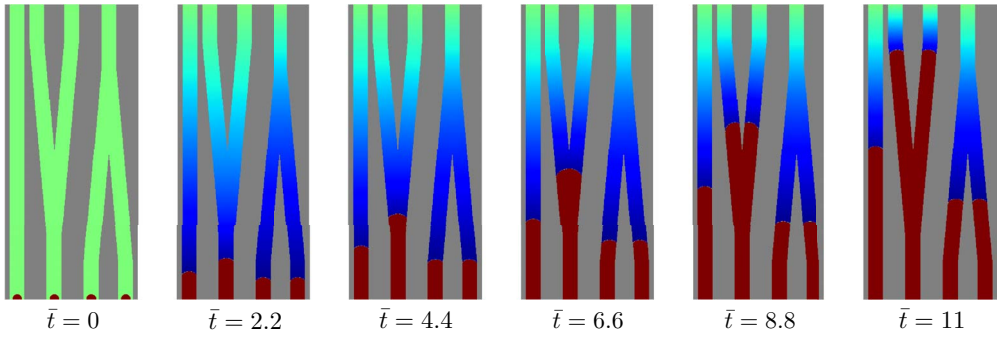

Figure 5. Series of representative configurations over time from a 2D phase-field simulation of nanowire growth in straight and branched pores demonstrating differences in growth rates for differently shaped pores.

The non-dimensional parameter s defined in Eq. 10 is a function of the pore geometry alone, and is a measure of how asymmetrically the pore cross-sectional area is distributed over the height of the pore. In the limit where $A(z)$ is everywhere close to its average value, s can be approximated as (see Appendix A for the derivation)

$$s \approx -\frac{4}{L}\left(\frac{\int_0^L zA(z)dz}{\int_0^L A(z)dz} - \frac{L}{2}\right) + 1, \qquad [11]$$

which states that s is proportional to the distance from the centroid of $A(z)$ to the center of the pore, so that if the centroid of $A(z)$ lies above (below) the midpoint of the pore, then $s < 1$ ($s > 1$).

For concreteness, we now consider a pore with linearly varying cross-sectional area, as shown schematically in 2D in Fig. 6a, where

$$A(z) = A_b\left[1 + \left(\frac{A_t}{A_b} - 1\right)\frac{z}{L}\right]. \qquad [12]$$

Here, A_t is the cross-sectional area at the top of the pore, and A_b is the cross-sectional area at the bottom of the pore, so $\frac{A_t}{A_b}$ characterizes how sloped the pore is. We perform numerical simulations of the 1D moving boundary problem defined by substituting Eq. 12 into Eq. 9, with boundary conditions at the electrodeposit-electrolyte interface given by Eqs. 2–4 for simulations labeled $\frac{i_i}{i_{lim}} < 1$ below. For simulations labeled $\frac{i}{i_{lim}} = 1$ below, we use the interfacial boundary condition $\hat{c} = 0$ instead of Eq. 2. Here, $i_{lim} = \frac{nFDc_{eq}}{L}$ is the limiting current density, and i_i is the initial current density associated with a given $\bar{\phi}_{el}$ assuming the concentration has instantly relaxed to a linear profile.

Figure 6b shows growth trajectories for $\frac{i}{i_{lim}} = 1$, when growth is limited entirely by diffusion. As expected, growth is faster in pores with larger values of $\frac{A_t}{A_b}$, which correspond to lower values of s and therefore lower values of $\frac{t_c}{t_{c,straight}}$. At the time when the pore with $\frac{A_t}{A_b} > 1$ becomes completely filled and would start forming a cap that blocks growth in surrounding pores, we can extract the normalized length $\frac{d_{straight}}{L}$ of a nanowire in a straight pore that began growing at the same time. This procedure can be repeated for various values of $\frac{A_t}{A_b}$ to determine what the length in a straight pore would be when a pore that promotes faster growth is filled and starts blocking its neighboring pores. Thus, if we assume that the average pore is perfectly straight, so that $s = 1$, then $\frac{d_{straight}}{L}$ represents the average non-dimensionalized nanowire length when a pore characterized by s is filled.

As shown in Fig. 6c, for $\frac{i}{i_{lim}} = 1$, $\frac{d_{straight}}{L}$ decreases rapidly as s departs from 1. We also perform simulations where $\frac{i_i}{i_{lim}} < 1$ by using the Butler-Volmer equation as an interfacial boundary condition and applying different potentials. As $\frac{i_i}{i_{lim}}$ is decreased by lowering the magnitude of the applied potential, growth becomes less diffusion-limited and $\frac{d_{straight}}{L}$ increases, so that variations in s have less influence on nanowire lengths. This is consistent with previous theoretical modeling[8] as well as experimental observations that reducing the overpotential or using pulsed potentials, which reduce how diffusion-limited the growth is, improves the homogeneity of nanowire lengths.[4,8,18]

Indeed, previous studies have drawn attention to the importance of template uniformity,[4,8] and templates with more disordered pores have been experimentally observed to lead to more non-uniform electrodeposition.[43] Our results highlight that the property of the template pores that determines the growth rate is the parameter s

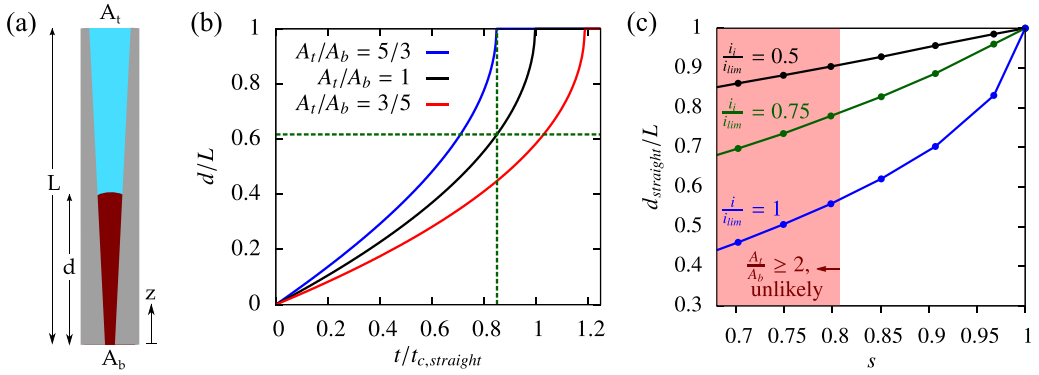

Figure 6. (a) Schematic of a pore with cross-sectional area that varies with height z. (b) Comparison of how nanowire length varies over time in pores with different cross-sectional area profiles. The vertical dashed line indicates the time when the deposit in a pore with $\frac{A_t}{A_b} = \frac{5}{3}$ reaches the end of the pore and the horizontal dashed line indicates the position of a nanowire in a straight pore at that time. (c) Position of a nanowire in a straight pore at the time a nanowire in a pore with $\frac{A_t}{A_b} \geq 1$ has reached the end of the template, as a function of s for the pore with $\frac{A_t}{A_b} \geq 1$. The red shaded region indicates the regime where $\frac{A_t}{A_b} \geq 2$, which correspond to large slopes that are unlikely in practice.

defined in Eq. 10, which characterizes the asymmetry in the distribution of pore cross-sectional area over the height of the template. Additionally, since Fig. 6c shows that the average scaled nanowire length $\frac{d_{straight}}{L}$ does not fall below approximately 0.4 even when s takes on rather extreme values, we can deduce that pore cross-sectional area variations are unlikely to fully explain the large nanowire length differences that have been observed experimentally in bismuth and bismuth-tin alloys[12,33] as well as copper deposited at large overpotentials into high-aspect-ratio pores.[8]

Framework for Statistical Analysis of Nanowire Length Distributions

Having studied nanowire growth via electrodeposition within templates comprising a small number of pores, we now turn to the behavior of statistically large collections of electrodeposited nanowires. Specifically, we develop a framework for analyzing nanowire length distributions, which may be extracted from experimental images such as those commonly reported in the literature.[3,8,12,39,44,45] First, we use various statistical methods to assess whether nanowire length distributions that appear to have two separate peaks are better modeled as bimodal or right-skewed unimodal. Then, we use standard tools from probability theory to extract the probability distributions of nucleation times or growth rates that would lead to a given nanowire length distribution.

Nanowire length distribution: bimodal vs. unimodal.—For concreteness, we focus on the experimental SEM image from Ref. 44 reproduced in Fig. 7a, which shows platinum nanowires in a cross-section of AAO template. We measure the nanowire lengths by manually tracing each nanowire in the image-analysis software FIJI[46] to obtain a representative dataset of nanowire lengths. We estimate the average total length using an accompanying lower-magnification SEM image (Fig. 2a in Ref. 44) that shows the entire length of the nanowires. Note that there is a significant amount of uncertainty in our length measurements as it is difficult to distinguish individual nanowires in the image and the sample size is small, so these measurements are primarily meant to demonstrate our proposed framework rather than to precisely analyze particular experimental results. An ideal image for extracting nanowire length distributions would allow a single row of individual nanowires to be clearly resolved so that the length of each nanowire can be accurately measured.

Frequently, the electrodeposition of nanowires appears to proceed with a double growth front,[4,8,44] but it is not clear whether there are indeed two separate peaks in the nanowire length distribution or whether the small number of longer nanowires comprise the tail of a skewed single-peaked distribution. If the distribution were bimodal, that may suggest the presence of multiple mechanisms for length differences or that different subpopulations of nanowires experience different nucleation or growth conditions. Previous analyses of the distribution of overgrowth cap areas for copper electrodeposited in AAO templates found cap areas to be bimodal for high ion concentrations,[31] but caps only reveal information about deposits that have reached the end of the template. Here we compute several statistical measures of unimodality for nanowire length distributions extracted from images of partially filled pores.

First, we compare the Akaike Information Criterion (AIC) of a Gaussian mixture model and a log-normal model. AIC is a method based on information theory for selecting a "best approximating model", where an AIC value is computed for each candidate model and the model with the minimum AIC value is considered the best.[47] We use the "mclust" package in R[48] to fit a mixture of two Gaussian distributions to the nanowire length data, as shown in Fig. 7b. We then fit the same nanowire length data to a single log-normal distribution using the "fitdistr" function in the "MASS" package in R,[49] as shown in Fig. 7c. From the log-likelihoods of the models, we calculate for each model the corrected Akaike Information Criterion $AIC_c = -2\ln L_m + 2k + \frac{2k(k+1)}{n-k-1}$, where L_m is the maximum likelihood of the model, k is the number of model parameters,

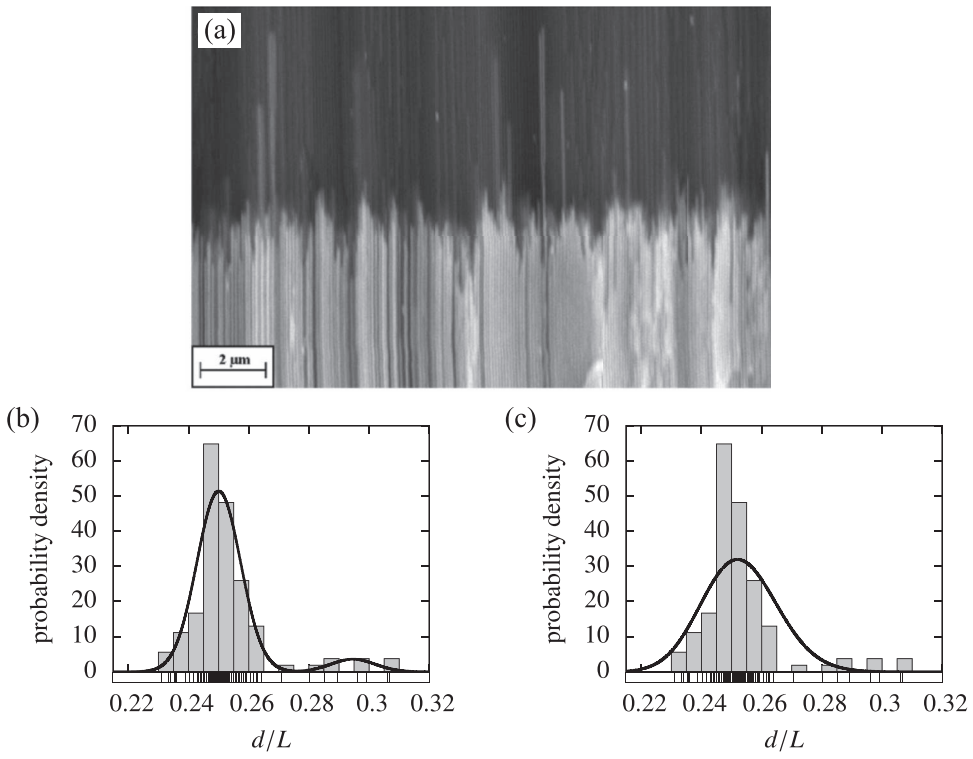

Figure 7. (a) Experimental SEM image of the ends of platinum nanowires (light) in an AAO template (dark), reproduced with permission from Ref. 44. (b) Scaled histogram of nanowire lengths with a scatterplot of the lengths shown under the x-axis. The black curve is a fitted mixture of two Gaussians. (c) Same scaled histogram and scatterplot of nanowire lengths, shown with fitted log-normal distribution.

Table I. Summary of transformations between a nanowire length distribution and a distribution of either nucleation times or pore-filling times. The transformation functions are derived from the growth trajectory $\frac{d(t)}{L} = 1 - \sqrt{1 - \frac{(t-t_{nucl})}{t_c}}$, and the transformation is calculated via $f_X(x) = \left|\frac{dg}{dx}\right| f_Y(g(x))$, where f_Y is a known probability density function of nanowire lengths.

variable	nucleation time	pore-filling time
transformation function	$g(x) = 1 - \sqrt{1 - \left(\frac{t_{eval}}{t_c} - x\right)}$	$g(x) = 1 - \sqrt{1 - \frac{(t_{eval}-t_{nucl})}{t_{c,peak}}\frac{1}{x}}$
x	$\frac{t_{nucl}}{t_c}$	$\frac{t_c}{t_{c,peak}}$
constant parameter	$\frac{t_{eval}}{t_c}$	$\frac{(t_{eval}-t_{nucl})}{t_{c,peak}}$

and n is the number of data points.[47] We find that $AIC_{c,1} = -697$ for the Gaussian mixture model and $AIC_{c,2} = -636$ for the log-normal model, from which we calculate that the respective Akaike weights $w_i = \frac{\exp(-\Delta_i/2)}{\sum_{r=1}^{R}\exp(-\Delta_r/2)}$ where $\Delta_i = AIC_{c,i} - AIC_{c,min}$ are $w_1 = 1 - 4.3 \times 10^{-14}$ and $w_2 = 4.3 \times 10^{-14}$. The significantly higher Akaike weight of the Gaussian mixture model suggests that it is much more likely than the log-normal model to explain the observed data.

To test for unimodality more generally using non-parametric approaches, we perform Silverman's kernel density estimate multimodality test with Hall and York's adjustment using the "silvermantest" package in R.[50–52] We find that the p-value is $p = 0.010 < 0.05$, so we reject the null hypothesis that the nanowire length distribution is unimodal. Finally, we perform Hartigans' dip test using the "diptest" package in R.[53,54] The dip test gives a p-value of $p = 0.996$, which does not support rejecting the null hypothesis that the distribution is unimodal. Keeping in mind that these non-parametric tests are quite conservative, we conclude from our three analyses that the nanowire distribution studied here is most likely bimodal, but we note that modality assessment is in general a challenging problem that is rendered particularly difficult here due to the small number of data points and the uncertainty in the data. In order to classify a nanowire length distribution as bimodal with greater certainty, experimental images that yield a larger number of nanowire length measurements, with greater accuracy, are needed.

Determining nucleation time or growth rate distributions from nanowire length distributions.—Next, we determine the variations in nucleation times or growth rates that would be required to lead to an observed distribution of nanowire lengths. Here we assume that each nanowire grows independently and the length of each nanowire varies with time according to Eq. 13 below, which was derived in Ref. 12 and holds for 1D growth limited only by diffusion:

$$d(t) = L - \sqrt{L^2 - 4\beta^2 D(t - t_{nucl})}, \qquad [13]$$

where β satisfies $\beta e^{-\beta^2}\text{erfi}(\beta) = \frac{c_{eq}}{c_s\sqrt{\pi}}$, d is the nanowire length, L is the pore length, t_{nucl} is the time at which nucleation occurs, and $\text{erfi}(\beta) = \frac{2}{\sqrt{\pi}}\int_0^\beta e^{t^2}dt$ is the imaginary error function. This growth trajectory can be written in non-dimensionalized form as

$$\frac{d(t)}{L} = 1 - \sqrt{1 - \frac{(t - t_{nucl})}{t_c}}, \qquad [14]$$

where $t_c = \left(\frac{L}{2\beta\sqrt{D}}\right)^2$ is the time it takes for the deposit to reach the end of the pore. Here, only growth inside the pore is considered, so $0 \le \frac{d}{L} \le 1$ and $0 \le \frac{t-t_{nucl}}{t_c} \le 1$.

Equation 14 describes the dependence of nanowire length on nucleation time and growth rate, which in turn depends on D through t_c. In order to use Eq. 14 to relate probability distributions of these values, Eq. 14 can be viewed as a one-to-one transformation $Y = g(X)$ that maps a random variable X, such as the nucleation time or pore-filling time, to a resulting random variable Y, such as the non-dimensionalized nanowire length. If the probability density function of the variable X is given by $f_X(x)$, so that the probability that $a \le X \le b$ is

$$P(a \le X \le b) = \int_a^b f_X(x)dx, \qquad [15]$$

then the probability density function of Y is given by the transformation of variables formula[55]

$$f_Y(y) = \frac{f_X(x)}{\left|\frac{dg}{dx}\right|}, \qquad [16]$$

where

$$x = g^{-1}(y), \qquad [17]$$

and the probability that $g(a) \le Y \le g(b)$ is

$$P(g(a) \le Y \le g(b)) = \int_{g(a)}^{g(b)} f_Y(y)dy. \qquad [18]$$

The reverse transformation, from a probability density function of Y to X, is thus given by

$$f_X(x) = \left|\frac{dg}{dx}\right| f_Y(g(x)). \qquad [19]$$

Here we will consider transformations of two possible variables, as summarized in Table I and explained further below.

First, let us calculate the nucleation time distribution corresponding to a given nanowire length distribution, assuming all variations in nanowire lengths are due to differences in nucleation times. Thus, we assume that t_{nucl} may vary for different pores, but t_c is the same for all pores. Let $f_Y(y)$ be the nanowire length distribution and let $f_X(x)$ be the corresponding distribution of nucleation times. Thus, $x = \frac{t_{nucl}}{t_c}$ represents the non-dimensionalized nucleation time, $y = \frac{d}{L}$ represents the non-dimensionalized nanowire length, and we additionally define $\frac{t_{eval}}{t_c}$ to be the non-dimensionalized time at which the nanowire lengths are evaluated. The transformation function is therefore

$$g(x) = 1 - \sqrt{1 - \left(\frac{t_{eval}}{t_c} - x\right)}. \qquad [20]$$

Figure 8a shows the nanowire length distribution that we will consider as an example here, namely the mixture of two Gaussians fitted above. Using Eqs. 19 and 20, we transform the fitted probability density function of nanowire lengths to find its corresponding nucleation time distribution, which is shown in Fig. 8b. Here we use $\frac{t_{eval}}{t_c} = 0.537$, which corresponds to the time since nucleation of the longest nanowire for which the probability density function is greater than 0.01. Note that integrating the nucleation time distribution gives the fraction of all nanowires that have nucleated as a function of time, as shown in Fig. 8c. We characterize the characteristic time over which nucleation occurs using the full-width half-maximum (FWHM) of the larger peak of the nucleation time distribution, and here we find that nucleation occurred over 2.6% of the pore-filling time. We can compare this value to the nucleation time scale inferred from early-time current transients, since the time over which the total current at early times experiences a peak indicates the time over which nucleation is

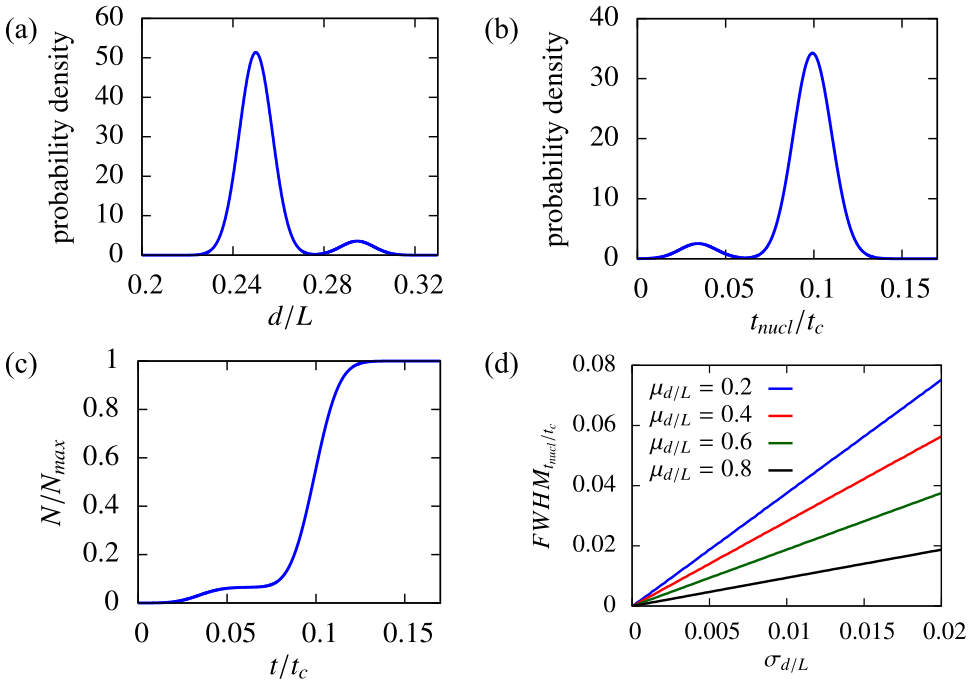

Figure 8. (a) Input distribution of nanowire lengths at time $\frac{t_{eval}}{t_c} = 0.537$, (b) corresponding distribution of nucleation times, and (c) number of nuclei as a function of time, computed from the nucleation time distribution. (d) The time scale over which nucleation occurs increases with standard deviation in nanowire lengths, assuming Gaussian distributions of nanowire lengths.

occurring.[3,56] Experimentally observed early-time current transients in the literature suggest that most nucleation occurs within the first 0.1% of the total pore-filling time.[3] Therefore, for the data analyzed here, entirely attributing the observed spread in nanowire lengths to a spread in nucleation times would significantly overestimate the time over which nucleation occurred.

More generally, we can calculate the spread in nucleation times necessary to produce a Gaussian distribution of nanowire lengths with arbitrary mean $\mu_{d/L}$ and standard deviation $\sigma_{d/L}$, as shown in Fig. 8d. Here, we again characterize the spread in nucleation times by the FWHM of the peak of the probability density function of $\frac{t_{nucl}}{t_c}$, denoted $FWHM_{t_{nucl}/t_c}$. Figure 8d thus predicts the spread in nucleation times that corresponds to a given nanowire length distribution, assuming differences in nucleation times are the only cause of nanowire length differences and growth conditions are entirely diffusion-limited. As expected, the spread in nucleation times increases as $\sigma_{d/L}$ increases, and the spread in nucleation times decreases as $\mu_{d/L}$ increases, since nanowire growth accelerates over time so the spread in nanowire lengths increases as the average length increases.

Next, let us instead assume that all variations in nanowire lengths arise due to differences in growth rates, in order to investigate resulting growth rate distributions. That is, we assume that $t - t_{nucl}$ is the same in all pores, while the pore-filling time t_c may take on different values in different pores. We also assume that growth in all of the pores still follows Eq. 14 so that t_c alone is sufficient to characterize growth rates (see Appendix C for analysis of this assumption). Figure 9a shows schematically the transformation from a distribution of nanowire lengths to a distribution of pore-filling times. To facilitate interpretation of pore-filling time distributions, we scale times by $t_{c,peak}$, which we define as the value of t_c that corresponds to the nanowire length d_{peak} of maximum probability density, and we rewrite the nanowire growth trajectory as

$$\frac{d(t)}{L} = 1 - \sqrt{1 - \frac{(t - t_{nucl})}{t_{c,peak}} \frac{t_{c,peak}}{t_c}}. \qquad [21]$$

Given a nanowire length distribution, we first calculate the value of the scaled time since nucleation $\frac{(t_{eval} - t_{nucl})}{t_{c,peak}}$ using $\frac{(t_{eval} - t_{nucl})}{t_{c,peak}} = 1 - \left(\frac{d_{peak}}{L} - 1\right)^2$. Then, we can use the transformation

$$g(x) = 1 - \sqrt{1 - \frac{(t_{eval} - t_{nucl})}{t_{c,peak}} \frac{1}{x}} \qquad [22]$$

to transform from the probability density function $f_Y(y)$ of the non-dimensionalized nanowire length $y = \frac{d}{L}$ to the probability density function $f_X(x)$ of the relative pore-filling time $x = \frac{t_c}{t_{c,peak}}$.

Let us again use as an illustrative example the mixture of two Gaussians fitted above, which is plotted again in Fig. 9b. Using Eq. 22 and Eq. 19, we determine the distribution of $\frac{t_c}{t_{c,peak}}$ that corresponds to the given distribution of nanowire lengths, as shown in Fig. 9c. If we assume that variations in pore-filling times are entirely attributable to variations in the template morphology, and we further assume that $t_{c,peak} = t_{c,straight}$, then the distribution shown in Fig. 9c is equivalent to the distribution of s, where s (defined in Eq. 10) is a measure of the asymmetry of the pore cross-sectional area profile along the height of the pore. Thus, assuming $\frac{t_c}{t_{c,peak}} = s$, the small spread in each of the peaks shown in Fig. 9c appears reasonable for the well-ordered AAO template that was used in the experiments. In conjunction with the analysis of nucleation times above, we conclude that for the data analyzed here, variations in pore geometry are a more plausible cause of the observed spread in each peak of the nanowire lengths than variations in nucleation times. This is also consistent with the fact that other experiments[12,15] that used more disordered templates observed significantly larger spreads in nanowire lengths than in the example studied here.

In order to predict distributions of pore-filling times more generally, we calculate the spread in $\frac{t_c}{t_{c,peak}}$ necessary to produce Gaussian distributions of nanowire lengths with arbitrary means $\mu_{d/L}$ and standard deviations $\sigma_{d/L}$, as shown in Fig. 9d. Again, if we assume that $\frac{t_c}{t_{c,peak}} = s$, then, similarly to Fig. 8d, Fig. 9d predicts the minimum amount of template inhomogeneity required to produce an observed

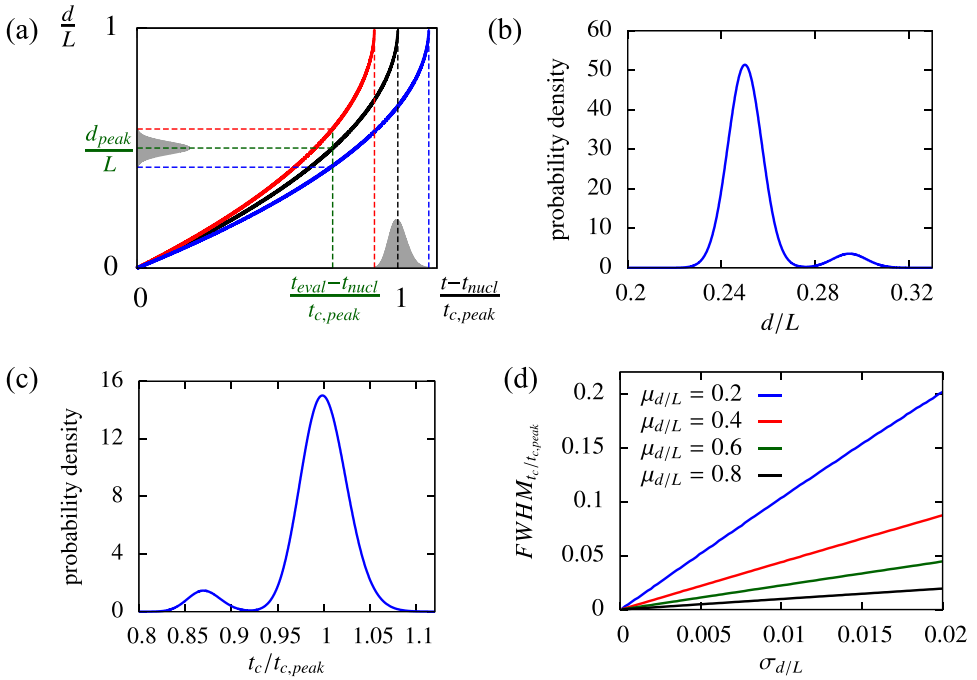

Figure 9. (a) Schematic illustration of a distribution of scaled nanowire lengths with peak at $\frac{d_{peak}}{L}$, corresponding scaled time $\frac{(t_{eval}-t_{nucl})}{t_{c,peak}}$, and corresponding distribution of scaled pore-filling times $\frac{t_c}{t_{c,peak}}$. (b) Input distribution of scaled nanowire lengths. (c) Corresponding distribution of scaled pore-filling times. (d) Spread in $\frac{t_c}{t_{c,peak}}$ increases with standard deviation of nanowire lengths, assuming distributions of $\frac{d}{L}$ are Gaussian. Assuming all variations in growth rates are due to pore geometry and assuming $t_{c,peak} = t_{c,straight}$ implies that $\frac{t_c}{t_{c,peak}} = s$.

distribution of nanowire lengths characterized by $\mu_{d/L}$ and $\sigma_{d/L}$, which can be roughly estimated by inspection from experimental SEM images. If it were possible to experimentally control and measure the distribution of pore shapes, then a comparison of the measured and predicted s distributions would allow our predictions to be tested, yielding insight on whether differences in pore geometry indeed contribute significantly to nanowire length variations.

In summary, by assuming that growth in each pore is independent and follows a particular trajectory, we have shown that simple transformations can be used to relate nanowire length distributions to corresponding distributions of either nucleation times or growth rates. By comparing these predicted distributions to experimental measurements using different techniques, the assumptions used in the transformations can be tested and a better understanding of nucleation and growth in these systems can be developed. Here, we have assumed that nanowires follow an entirely diffusion-limited growth trajectory that does not account for parameters such as the applied potential and is only very weakly dependent on the electrolyte concentration. Since both overpotential and electrolyte concentration have been observed to significantly affect nanowire length uniformity,[57] we expect that accounting for these effects would further improve the accuracy of the distribution predictions. For example, lower overpotentials would lead to less diffusion-limited conditions and thus less acceleration during growth, so that greater pore-to-pore variations in nucleation times or growth rates would be necessary to cause a given spread in nanowire lengths. On the other hand, in practice it is likely that multiple effects combine to cause a given spread in nanowire lengths, so that small variations in each individual factor may be sufficient to lead to significant nanowire length inhomogeneity.

Another mechanism for pore-to-pore variations in nanowire lengths that we have not accounted for is the presence of side reactions. We hypothesize that side reactions may explain nanowire length differences that are too large to be explained by other mechanisms, since side reactions may slow growth in a majority of pores by, for example, blocking the pores with gas bubbles, while growth rates remain significantly higher in a small number of unaffected pores. Experimentally it has been found that bubbles formed from hydrogen reduction can inhibit the growth of nickel nanowires deposited at high overpotentials,[38] and visible gas generation has been observed at high overpotentials.[3] In addition, experimentally observed early-time current transients that exhibit different behavior at different temperatures, along with a decrease in nanowire length uniformity at higher temperatures,[15] may be evidence of thermally activated side reactions that affect nanowire growth. Thus, the possibility of side reactions should be accounted for when analyzing nanowire electrodeposition, especially at high overpotentials.

Conclusions

In this paper we have developed a phase-field model for template-assisted electrodeposition and demonstrated methods for analyzing nanowire length distributions that lead to a better understanding of non-uniform deposit growth. Using 2D and 3D phase-field simulations, we studied the fraction of pore width filled under various conditions and reproduced characteristic current transients as well as morphologies that have been observed experimentally when electrodeposits overflow a template. Our simulations also showed that non-zero diffusivity of the template material leads to increased non-uniformity in nanowire lengths due to a shielding effect that leads to competitive growth. Next, we found that the time required to fill a pore of arbitrary shape is determined by a parameter that characterizes the asymmetry in the pore cross-sectional area profile over the height of the template, so that template inhomogeneities can contribute significantly to differences in nanowire lengths. Finally, we demonstrated methods for analyzing nanowire length distributions that can be extracted from experimental SEM images. We investigated whether a nanowire length distribution was better modeled as bimodal or right-skewed unimodal, and we used transformations of probability distributions to calculate the spreads in nucleation times or growth rates necessary to cause given spreads in nanowire lengths.

Our nanowire length distribution transformations led us to conclude that, for the example from the literature that we considered, the spread in the majority of nanowire lengths is most likely caused primarily by a spread in growth rates rather than a spread in nucleation times. More broadly, we hope that the theoretical predictions presented here can be used in conjunction with experimental measurements of nanowire lengths, nucleation times, and pore geometry variations to better understand template-assisted electrodeposition. In closing, we emphasize that the analysis presented here is applicable not only to electrodeposition in porous templates but also to the growth of materials in any system where interfacial evolution in a confined geometry is determined by an interplay of diffusion and reaction kinetics.

Acknowledgments

A. F. acknowledges a National Science Foundation Graduate Research Fellowship under grant No. DGE 1148900. Useful discussions with Ryan Davis, Sangwoo Shin, Howard Stone, and Yuanda Xu are gratefully acknowledged.

Appendix A: Derivations of Expressions for Pore-Filling Time for Arbitrary Cross-Sectional Area Profiles

Derivation of expression for s.—Here we derive an expression for the time t_c to fill a pore with cross-sectional area profile $A(z)$, relative to the pore-filling time of a straight pore $t_{c,straight}$. Assuming $\frac{c_s}{c_{eq}} \gg 1$ so that $\hat{c}(z)$ instantaneously attains its steady-state profile at each time, Eq. 9 reduces to

$$\frac{d}{dz}\left[DA(z)\frac{d\hat{c}}{dz}\right] = 0. \quad [A1]$$

Assuming entirely diffusion-limited conditions yields the boundary conditions $\hat{c}(z = l) = 0$ and $\hat{c}(z = L) = c_{eq}$, where l is the length of the nanowire. Integrating Eq. A1 twice and applying the boundary conditions yields

$$\hat{c}(z) = \frac{c_{eq}}{\int_l^L \frac{1}{A(z')}dz'}\int_l^z \frac{1}{A(z')}dz'. \quad [A2]$$

Equations 3 and 4 can be combined and written in 1D form to yield

$$\frac{dl}{dt} = \frac{D}{c_s}\frac{d\hat{c}}{dz}\bigg|_{z=l}. \quad [A3]$$

Substituting the derivative of Eq. 24 evaluated at $z = l$ into Eq. A3 and integrating the resulting separable differential equation gives:

$$\frac{dl}{dt} = \frac{D}{c_s}\frac{c_{eq}}{\int_l^L \frac{1}{A(z')}dz'}\frac{1}{A(l)}, \quad [A4]$$

or

$$\int_0^L \left(A(l)\int_l^L \frac{1}{A(z')}dz'\right)dl = \frac{Dc_{eq}}{c_s}\int_0^{t_c} dt, \quad [A5]$$

or

$$t_c = \frac{c_s}{Dc_{eq}}\int_0^L \left(A(l)\int_l^L \frac{1}{A(z')}dz'\right)dl. \quad [A6]$$

Finally, normalizing by $t_{c,straight} = \frac{L^2 c_s}{2c_{eq}D}$ and writing z instead of l for clarity gives

$$\frac{t_c}{t_{c,straight}} = s \quad [A7]$$

where

$$s \equiv \frac{2}{L^2}\int_0^L \left(A(z)\int_z^L \frac{1}{A(z')}dz'\right)dz. \quad [A8]$$

Derivation of approximate expression for s.—Here we derive an approximate expression for s under the assumption that $A(z) \approx \frac{\int_0^L A(z)dz}{L} \equiv \bar{A}$, so that $A(z)$ is everywhere close to its average value. This implies that we can Taylor expand $\frac{1}{A(z)}$ to yield:

$$\frac{1}{A(z)} = \frac{1}{\bar{A}} + (A(z) - \bar{A})\left(\frac{-1}{\bar{A}^2}\right) + \mathcal{O}((A(z) - \bar{A})^2) \quad [A9]$$

$$\approx \frac{2}{\bar{A}} - \frac{A(z)}{\bar{A}^2}. \quad [A10]$$

Substituting Eq. A10 into Eq. 10 gives

$$s \approx \frac{2}{L^2}\int_0^L \left(A(z)\int_z^L \left[\frac{2}{\bar{A}} - \frac{A(z')}{\bar{A}^2}\right]dz'\right)dz \quad [A11]$$

$$\approx \frac{2}{L^2}\left(\int_0^L A(z)\frac{2}{\bar{A}}(L - z)dz - \frac{\int_0^L A(z)\int_z^L A(z')dz'dz}{\bar{A}^2}\right) \quad [A12]$$

$$\approx \frac{2}{L^2}\left(2L^2 - \frac{2\int_0^L zA(z)dz}{\bar{A}} - \frac{L^2}{2}\right) \quad [A13]$$

$$\approx -\frac{4}{L}\frac{\int_0^L zA(z)dz}{\int_0^L A(z)dz} + 3 \quad [A14]$$

$$\approx -\frac{4}{L}\left(\frac{\int_0^L zA(z)dz}{\int_0^L A(z)dz} - \frac{L}{2}\right) + 1, \quad [A15]$$

where we used $\frac{\int_0^L A(z)\int_z^L A(z')dz'dz}{(L\bar{A})^2} = \frac{1}{2}$, which is shown next.

Let $F(z) = \int^z A(z')dz'$. Then,

$$\frac{\int_0^L A(z)\int_z^L A(z')dz'dz}{\left(\int_0^L A(z)dz\right)^2} = \frac{\int_0^L F'(z)[F(L) - F(z)]dz}{[F(L) - F(0)]^2} \quad [A16]$$

$$= \frac{F(L)[F(L) - F(0)] - \int_0^L F'(z)F(z)dz}{[F(L) - F(0)]^2} \quad [A17]$$

$$= \frac{F(L)[F(L) - F(0)] - \frac{F(L)^2 - F(0)^2}{2}}{[F(L) - F(0)]^2} \quad [A18]$$

$$= \frac{1}{2} \quad [A19]$$

Appendix B: Comparison of Planar Phase-Field Simulations, 1D Sharp-Interface Simulations, and Analytical Solutions

In order to validate our phase-field and 1D sharp-interface simulations, we compare numerical simulation results to the analytical solution from Ref. 12, which is valid in the limit of completely diffusion-limited growth:

$$\frac{d(t)}{L} = 1 - \sqrt{1 - \frac{t}{t_c}} \quad [B1]$$

where $t_c = \left(\frac{L}{2\beta\sqrt{D}}\right)^2$ and β satisfies $\beta e^{-\beta^2}\text{erfi}(\beta) = \frac{c_{eq}}{c_s\sqrt{\pi}}$. The corresponding magnitude of the current density is:

$$|i(t)| = \frac{n\mathcal{F}c_s L}{2t_c\sqrt{1 - \frac{t}{t_c}}}. \quad [B2]$$

At early times when $t < t_{lim} \equiv \frac{L^2}{\pi D}$, we also compare our numerical simulations to the Cottrell equation:[56]

$$|i_{Cottrell}(t)| = \frac{n\mathcal{F}c_{eq}\sqrt{D}}{\sqrt{\pi t}} \quad [B3]$$

and its corresponding equation for position as a function of time:

$$\frac{d_{Cottrell}(t)}{L} = \frac{2c_{eq}\sqrt{Dt}}{c_s L\sqrt{\pi}}. \quad [B4]$$

Figure BI shows comparisons of the numerical simulations with the analytical expressions over the entire growth time as well as at early times. For the numerical simulations, $\tilde{\phi}_{el} = -13$ was used in order to simulate highly diffusion-limited conditions.

Appendix C: Nanowire Growth in Pores with Varying Cross-Sectional Areas

We justify using only t_c to characterize growth rates in pores with different linearly varying cross-sectional area profiles because the growth trajectories of the differently sloped pores are nearly the same when time is scaled by each respective pore-filling time t_c, as shown in Fig. C1a. We also perform 1D sharp-interface simulations to determine the pore-filling time for different forms of $A(z)$, as shown in Fig. C1b, and confirm that $\frac{t_c}{t_{c,straight}} = s$. In addition to pores with linearly varying areas over the entire height of the template, we considered pores that are linearly sloped over only a fraction of the height

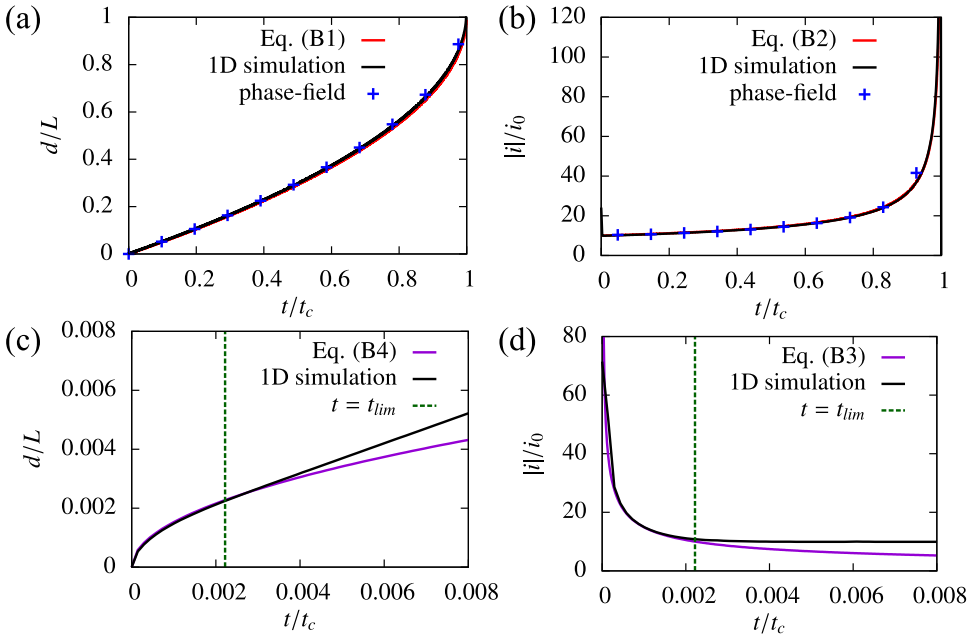

Figure B1. (a) Comparison of scaled nanowire length $\frac{d}{L}$ as a function of scaled time $\frac{t}{t_c}$ from a planar 2D phase-field simulation, a 1D numerical simulation of the sharp-interface equations, and Eq. B1. (b) Comparison of the corresponding scaled current density magnitude vs. scaled time. (c) Comparison at early times of scaled nanowire length vs. scaled time for a 1D sharp-interface simulation and the growth trajectory implied by the Cottrell equation. (d) Comparison at early times of the corresponding scaled current density magnitude vs. scaled time.

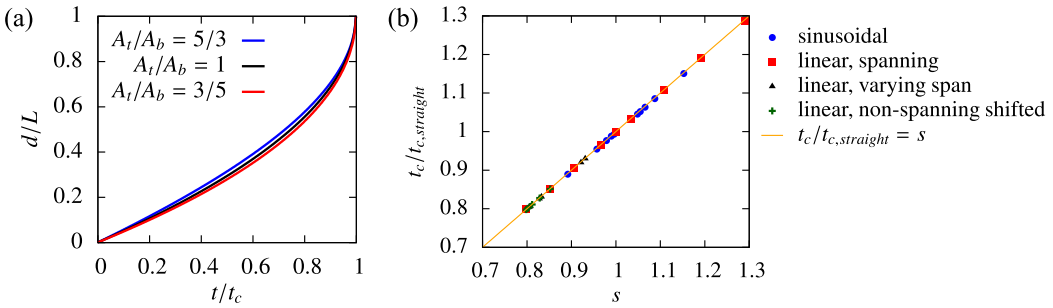

Figure C1. (a) $\frac{d}{L}$ vs. $\frac{t}{t_c}$ for linearly sloped pores with different values of $\frac{A_t}{A_b}$. (b) $\frac{t_c}{t_{c,straight}}$ vs. s for pores with different forms of $A(z)$.

of the template, while the remaining parts of the pore are straight and $A(z)$ is continuous. We also considered sinusoidally varying $A(z)$ with different wavelengths and with phases such that $A(z)$ is not symmetric about $\frac{z}{L} = 0.5$. Note that here we only show the time required to completely fill a pore. At intermediate times before the pore is completely filled, the position of the growth front varies substantially depending on the particular shape of the pore.

References

1. A. J. Yin, J. Li, W. Jian, A. J. Bennett, and J. M. Xu, *Appl. Phys. Lett.*, **79**, 1039 (2001).
2. L.-M. Lu, L. Zhang, F.-L. Qu, H.-X. Lu, X.-B. Zhang, Z.-S. Wu, S.-Y. Huan, Q.-A. Wang, G.-L. Shen, and R.-Q. Yu, *Biosens. Bioelectron.*, **25**, 218 (2009).
3. K. S. Napolskii, I. V. Roslyakov, A. A. Eliseev, D. I. Petukhov, A. V. Lukashin, S.-F. Chen, C.-P. Liu, and G. A. Tsirlina, *Electrochim. Acta*, **56**, 2378 (2011).
4. L. Trahey, C. R. Becker, and A. M. Stacy, *Nano Lett.*, **7**, 2535 (2007).
5. T. Ozel, G. R. Bourret, and C. A. Mirkin, *Nat. Nanotechnol.*, **10**, 319 (2015).
6. I. Enculescu, Z. Siwy, D. Dobrev, C. Trautmann, M. T. Molares, R. Neumann, K. Hjort, L. Westerberg, and R. Spohr, *Appl. Phys. A*, **77**, 751 (2003).
7. A. D. Davydov and V. M. Volgin, *Russ. J. Electrochem.*, **52**, 806 (2016).
8. A. A. Noyan, A. P. Leontiev, M. V. Yakovlev, I. V. Roslyakov, G. A. Tsirlina, and K. S. Napolskii, *Electrochim. Acta*, **226**, 60 (2017).
9. S. Shin and H. H. Cho, *Electrochim. Acta*, **117**, 120 (2014).
10. M. B. Khedim, L. Cagnon, C. Garagnon, V. Serradeil, and D. Bourgault, *Phys. Chem. Chem. Phys.*, **18**, 12332 (2016).
11. P. Bai, J. Li, F. R. Brushett, and M. Z. Bazant, *Energy Environ. Sci.*, **9**, 3221 (2016).
12. S. Shin, T. T. Al-Housseiny, B. S. Kim, H. H. Cho, and H. A. Stone, *Nano Lett.*, **14**, 4395 (2014).
13. D. A. Bograchev, V. M. Volgin, and A. D. Davydov, *Electrochim. Acta*, **112**, 279 (2013).
14. C. G. Jin, W. F. Liu, C. Jia, X. Q. Xiang, W. L. Cai, L. Z. Yao, and X. G. Li, *J. Cryst. Growth*, **258**, 337 (2003).
15. S. Shin, B. H. Kong, B. S. Kim, K. M. Kim, H. K. Cho, and H. H. Cho, *Nanoscale Res. Lett.*, **6**, 1 (2011).
16. S. Blanco, R. Vargas, J. Mostany, C. Borrás, and B. R. Scharifker, *J. Electrochem. Soc.*, **161**, E3341 (2014).
17. M. B. Hariri, A. Dolati, and R. S. Moakhar, *J. Electrochem. Soc.*, **160**, D279 (2013).
18. I. U. Schuchert, M. E. T. Molares, D. Dobrev, J. Vetter, R. Neumann, and M. Martin, *J. Electrochem. Soc.*, **150**, C189 (2003).
19. S. Valizadeh, J. M. George, P. Leisner, and L. Hultman, *Electrochim. Acta*, **47**, 865 (2001).
20. J. E. Guyer, W. J. Boettinger, J. A. Warren, and G. B. McFadden, *Phys. Rev. E*, **69**, 021604 (2004).
21. D. A. Cogswell, *Phys. Rev. E*, **92**, 011301 (2015).
22. L. Chen, H. W. Zhang, L. Y. Liang, Z. Liu, Y. Qi, P. Lu, J. Chen, and L.-Q. Chen, *J. Power Sources*, **300**, 376 (2015).
23. S. DeWitt, N. Hahn, K. Zavadil, and K. Thornton, *J. Electrochem. Soc.*, **163**, A513 (2016).
24. A. Jana, D. R. Ely, and R. E. García, *J. Power Sources*, **275**, 912 (2015).
25. Y. D. Gamburg and G. Zangari, *Theory and Practice of Metal Electrodeposition* (Springer Science & Business Media, 2011).
26. K. M. Takahashi and M. E. Gross, *J. Electrochem. Soc.*, **146**, 4499 (1999).
27. L.-G. Sundström and F. H. Bark, *Electrochim. Acta*, **40**, 599 (1995).
28. J. Newman and K. E. Thomas-Alyea, *Electrochemical Systems*, 3rd ed. (John Wiley & Sons, Inc., 2004).

29. J.-H. Han, E. Khoo, P. Bai, and M. Z. Bazant, *Sci. Rep.*, **4** (2014).
30. L. Liang and L.-Q. Chen, *Appl. Phys. Lett.*, **105**, 263903 (2014).
31. F. S. Fedorov, P. Dunne, A. Gebert, and M. Uhlemann, *J. Electrochem. Soc.*, **162**, D568 (2015).
32. S. Shin, B. S. Kim, K. M. Kim, B. H. Kong, H. K. Cho, and H. H. Cho, *J. Mater. Chem.*, **21**, 17967 (2011).
33. A. L. Prieto, M. Martín-González, J. Keyani, R. Gronsky, T. Sands, and A. M. Stacy, *J. Am. Chem. Soc.*, **125**, 2388 (2003).
34. C. P. Nielsen and H. Bruus, *Phys. Rev. E*, **92**, 052310 (2015).
35. W. N. Gill, D. J. Duquette, and D. Varadarajan, *J. Electrochem. Soc.*, **148**, C289 (2001).
36. P. G. Saffman and G. Taylor, *Proc. R. Soc. London, Ser. A*, **245**, 312 (1958).
37. M. Motoyama, Y. Fukunaka, Y. H. Ogata, and F. B. Prinz, *J. Electrochem. Soc.*, **157**, D357 (2010).
38. M. P. Proenca, C. T. Sousa, J. Ventura, M. Vazquez, and J. P. Araujo, *Electrochim. Acta*, **72**, 215 (2012).
39. A. P. Leontiev, O. A. Brylev, and K. S. Napolskii, *Electrochim. Acta*, **155**, 466 (2015).
40. M. E. T. Molares, V. Buschmann, D. Dobrev, R. Neumann, R. Scholz, I. U. Schuchert, and J. Vetter, *Adv. Mater.*, **13**, 5 (2001).
41. R. Zwanzig, *J. Phys. Chem.*, **96**, 3926 (1992).
42. A. Ledesma-Durán, S. I. Hernández-Hernández, and I. Santamaría-Holek, *J. Phys. Chem. C*, **120**, 7810 (2016).
43. Y. Dahmane, L. Cagnon, J. Voiron, S. Pairis, M. Bacia, L. Ortega, N. Benbrahim, and A. Kadri, *J. Phys. D: Appl. Phys.*, **39**, 4523 (2006).
44. K. S. Napolskii, P. J. Barczuk, S. Y. Vassiliev, A. G. Veresov, G. A. Tsirlina, and P. J. Kulesza, *Electrochim. Acta*, **52**, 7910 (2007).
45. W.-L. Wang, C.-C. Wan, and Y.-Y. Wang, *J. Phys. Chem. B*, **110**, 12974 (2006).
46. J. Schindelin, I. Arganda-Carreras, E. Frise, V. Kaynig, M. Longair, T. Pietzsch, S. Preibisch, C. Rueden, S. Saalfeld, B. Schmid, J.-Y. Tinevez, D. J. White, V. Hartenstein, K. Eliceiri, P. Tomancak, and A. Cardona, *Nat. Methods*, **9**, 676 (2012).
47. K. P. Burnham and D. R. Anderson, *Model Selection and Multimodel Inference: A Practical Information-Theoretic Approach*, 2nd ed. (Springer-Verlag, 2002).
48. C. Fraley and A. E. Raftery, *J. Am. Stat. Assoc.*, **97**, 611 (2002).
49. W. N. Venables and B. D. Ripley, *Modern Applied Statistics with S*, 4th ed. (Springer, 2002).
50. B. W. Silverman, *J. R. Stat. Soc. Ser. B Stat. Methodol.*, **43**, 97 (1981).
51. P. Hall and M. York, *Stat. Sin.*, **11**, 515 (2001).
52. F. Schwaiger and H. Holzmann, *silvermantest: Package which Implements the Silverman Test* (2013).
53. J. A. Hartigan and P. M. Hartigan, *Ann. Stat.*, **13**, 70 (1985).
54. M. Maechler, *diptest: Hartigan's Dip Test Statistic for Unimodality - Corrected* (2015).
55. M. A. Berger, *An Introduction to Probability and Stochastic Processes* (Springer Science & Business Media, 2012) p. 12.
56. D. Grujicic and B. Pesic, *Electrochim. Acta*, **47**, 2901 (2002).
57. H. R. Lim, S. Kim, Y.-I. Lee, K.-J. Lee, and Y.-H. Choa, *J. Electrochem. Soc.*, **161**, D442 (2014).